iScience

CellPress
OPEN ACCESS

Article

Immunomodulation and delivery of macrophages using nano-smooth drug-loaded magnetic microrobots for dual targeting cancer therapy

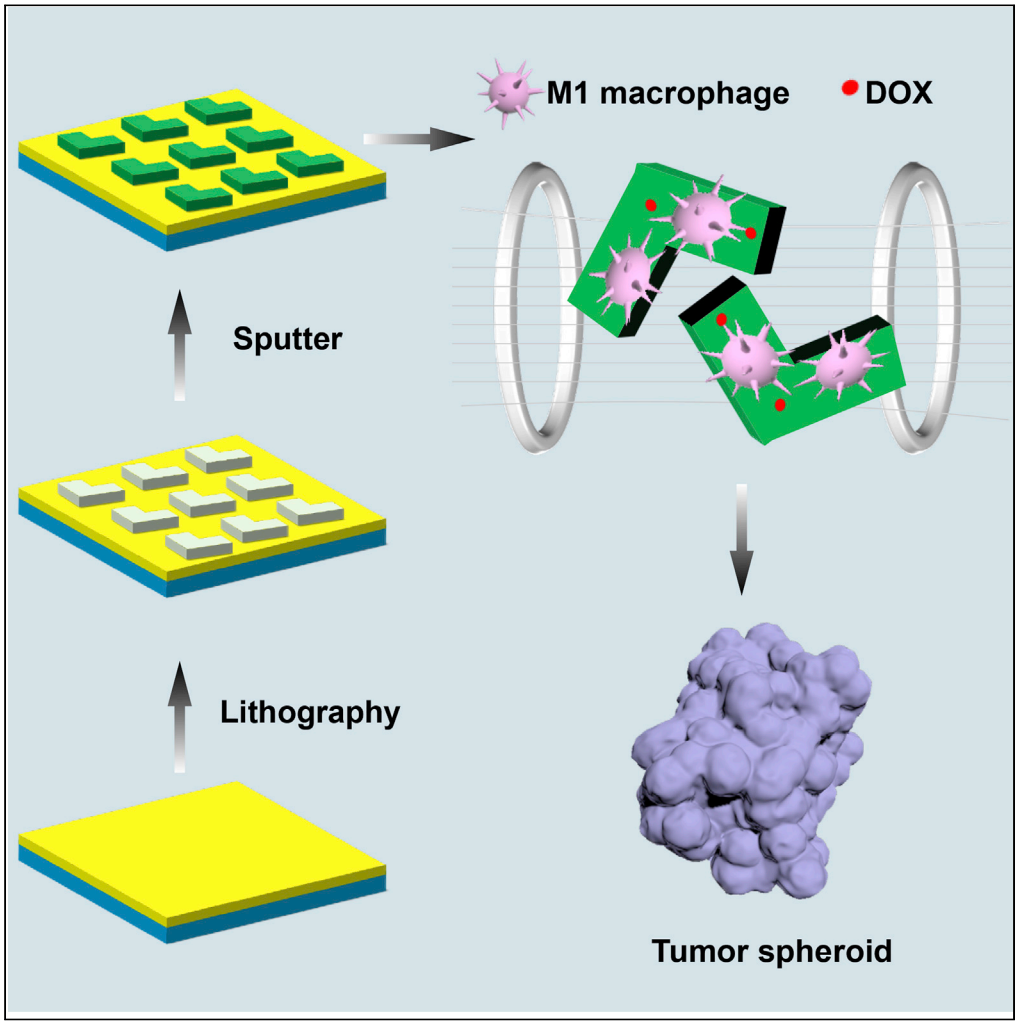

Xiaoxia Song, Wei Fu, U Kei Cheang

cheanguk@sustech.edu.cn

Highlights

Drug-loaded achiral magnetic microrobots developed with scalability and mass fabrication

Magnetic microrobot with nano-smooth surface can activate antitumor phenotype macrophage

The magnetic targeting and targeted therapy of polarized macrophages were combined

The magnetic microrobots exhibit enhanced tumor-targeting and antitumor capabilities

Song et al., iScience 25, 104507
July 15, 2022
https://doi.org/10.1016/j.isci.2022.104507

iScience

CellPress
OPEN ACCESS

Article

Immunomodulation and delivery of macrophages using nano-smooth drug-loaded magnetic microrobots for dual targeting cancer therapy

Xiaoxia Song,[1] Wei Fu,[1] and U Kei Cheang[1,2,3,4,*]

SUMMARY

To realize the potential to use micro/nanorobots for targeted cancer therapy, it is important to improve their biocompatibility and targeting ability. Here, we report on drug-loaded magnetic microrobots capable of polarizing macrophages into the antitumor phenotype to target and inhibit cancer cells. *In vitro* tests demonstrated that the microrobots have good biocompatibility with normal cells and immune cells. Positively charged DOX was loaded onto the surface of microrobots via electrostatic interactions and exhibited pH-responsive release behavior. The nano-smooth surfaces of the microrobots activated M1 polarization of macrophages, thus activating their intrinsic targeting and antitumor abilities toward cancer cells. Through dual targeting from magnetic guidance and M1 macrophages, the microrobots were able to target and kill cancer cells in a 3D tumor spheroid culture assay. These findings demonstrate a way to improve the tumor-targeting and antitumor abilities of microrobots through the combined use of magnetic control, macrophages, and pH-responsive drug release.

INTRODUCTION

Recent developments in untethered mobile micro/nanorobots offer viable solutions in the field of biomedicine, such as addressing the challenges in targeted cancer therapies. Their small size permits them to target narrow sites and play a therapeutic role in complex *in vivo* environments (Alapan et al., 2020; Miskin et al., 2020; Soto et al., 2020; Wang et al., 2021; Wu et al., 2020; Yan et al., 2019). The current research trend in micro/nanorobots is to focus on enhancing their functions to increase their therapeutic effects. Inspired by nature, a growing number of micro/nanorobots combined with live cells were designed with increased biocompatibility and applicability for *in vivo* applications (Berta Esteban-Fernandez de Avila et al., 2018; Buss et al., 2020; Felfoul et al., 2016; Huo et al., 2020; Magdanz et al., 2020; Xu et al., 2020b; Yan et al., 2017; Zhong et al., 2020). Eukaryotic cell-based microrobots fabricated via endocytosis of therapeutic nanoparticles or encapsulation by cell membrane are regarded as some of the most effective designs for cargo delivery and can potentially be widely applied to cancer detection, imaging, diagnosis, and therapy (Agrahari et al., 2020; Ebrahimi et al., 2021; Zhou et al., 2021). Their major advantage lies in their ability to be a masquerader to avoid clearance by the reticuloendothelial system, thus prolonging circulation time in blood and increasing therapeutic effectiveness (Fan et al., 2020; Nikitin et al., 2020; Zhai et al., 2017). For instance, the red blood cells (RBC) microrobots with internalized iron oxide nanoparticles actuated by ultrasound and magnetic field combine synthetic motors with long bloodstream circulation, safety, and versatile cargo-carrying capabilities of RBC (Wu et al., 2014, 2015). Furthermore, the RBC microrobots showed enhanced *in vitro* photodynamic therapy (PDT) effect through photosensitizer molecule (Gao et al., 2019). Recently, natural self-propelled sperm emerged as promising biohybrid microrobots for active targeting delivery. Recent work on the treatment of cervical and ovarian cancer spheroids using magnetically controlled guided sperm robots loaded with chemotherapeutic agents (Xu et al., 2018, 2020a) demonstrated the vast potential of eukaryotic cell-based microrobots for targeted cancer therapies.

With the fast developments in biology and medical science, immunotherapies using macrophages have advanced significantly over the past decades (Han et al., 2019). Monocyte-derived macrophages are the predominant immune cells that play important roles in inflammatory and neoplastic diseases (Ladanyi, 2015). Macrophages have a long blood circulation half-life and effective tumor-specific binding, making them a viable candidate for tumor therapy. Taking advantage of these properties, Han et al. developed

[1]Department of Mechanical and Energy Engineering, Southern University of Science and Technology, Shenzhen 518055, China

[2]Shenzhen Key Laboratory of Biomimetic Robotics and Intelligent Systems, Southern University of Science and Technology, Shenzhen, China

[3]Guangdong Provincial Key Laboratory of Human-Augmentation and Rehabilitation Robotics in Universities, Southern University of Science and Technology, Shenzhen, China

[4]Lead contact

*Correspondence: cheanguk@sustech.edu.cn

https://doi.org/10.1016/j.isci.2022.104507

microrobots that were synthesized by endocytosis of drug-loaded magnet nanoparticles by macrophages to target tumor spheroid in a microfluidic channel (Han et al., 2016). However, at the molecular level, engineered macrophages via endocytosis may result in the activation of the NF-kB pathways (Wang et al., 2014), which promotes tumor growth and angiogenesis (Luedde et al., 2007).

Macrophages are known to be double-edged swords for tumor therapy (Woo et al., 2015). Different macrophage phenotypes show varying effects on tumor immunity. Specifically, M1-polarized macrophages inhibited tumor growth via secreting chemokines, whereas M2 macrophages, which are tumor-associated macrophages (TAMs), promote tumor growth and metastasis (Hu et al., 2020; Xia et al., 2020; Yong et al., 2019). Therefore, it is important to activate the desirable macrophage phenotype in order to achieve a more positive effect in tumor therapy (Deng et al., 2019; Zhang et al., 2019). The phenotype of macrophages can be determined by the surface properties of the materials to which the macrophages adhered (Jin et al., 2019; Sahu et al., 2020). For example, macrophage growth along narrow grooves pattern substrate can promote M2 polarization (McWhorter et al., 2013). Furthermore, a rough surface can promote macrophage polarization toward the M2 phenotype, which will contribute to the regenerative capacity of tumors *in vitro* and *in vivo* (Song et al., 2021). On the other hand, a smooth surface can induce inflammatory M1 macrophage activation, and thus inhibit tumor growth via upregulated gene expression levels of interleukins IL-1β, IL-6, and tumor necrosis factor (TNFα) (Duan and Luo, 2021; Hotchkiss et al., 2016). It was reported that the surface roughness led to the activation of the macrophage's NF-κB signaling pathway, which is a possible explanation for the M1 polarization (Waterfield et al., 2010). Therefore, endowing magnetically actuated microrobots with surface properties that can regulate macrophage polarization will enhance their tumor targeting and treatment capabilities (Schmidt et al., 2020).

Magnetically driven achiral planar microrobots have garnered attention owing to their effective propulsive ability under rotating or conical magnetic field actuation (Cheang et al., 2014b, 2017; Cohen et al., 2019). In addition, propellers with achiral planar shapes offer the advantage of scalability and mass fabrication by circumventing the need to fabricate complex 3D structures while maintaining swimming speed that can compete with helical microrobots (Mirzae et al., 2018). Herein, a type of achiral microrobots (AMRs) modified from previous work (Cheang et al., 2014b, 2017) was fabricated using photolithography and magnetron sputter and then seeded with macrophage cells. The planar geometries of microrobots offer large flat surfaces for the uniform coating of the metal layers; thus, the fabricated AMRs can provide flat, nano-smooth surfaces that can induce the differentiation of M1 macrophages with a high expression of related cytokines, promoting their antitumor and tumor-targeting abilities. Furthermore, AMRs have negative zeta potential surfaces that enhanced the loading of positively charged doxorubicin (DOX) via electrostatic interactions and enabled pH-triggered drug release; this further improved the tumor-specific targeting function of the AMRs. Finally, the tumor-specific targeting of AMRs with M1 macrophages was verified in targeted drug delivery experiments using 3D tumor spheroids. Such microrobots with immunoregulation functionality will provide new insights into the development of functional microrobots with efficient tumor-targeting ability.

RESULTS

Fabrication and characterization of L magnet microrobot

AMRs coated with nickel (Ni) and titanium (Ti) layers with nano-smooth surfaces were successfully prepared using bottom-up fabrication processes, as shown in Figure 1A. First, a sacrificial dextran layer was spin coated on a cleaned Si wafer. Then, 5 μm thick achiral planar structures were fabricated using photolithography with negative photoresist (SU-8 2015). Next, 300 nm Ni and 30 nm Ti layers are coated on the SU-8 structures through magnetron sputtering; the Ni and Ti layers endowed the structures with magnetic and biocompatible properties, respectively. Although electron beam evaporation is more commonly used for coating micro/nanorobots, this technique might cause the metal coating to peel off when submerged in fluid for a long period of time (Zhang et al., 2018). To address this problem, magnetron sputtering was used to achieve more dense and adherent coatings.

Characteristics of the AMRs were investigated and are presented in Figures 1B–1J. Scanning electron microscopy (SEM) observations confirmed that the AMRs displayed smooth V-like shapes with arm lengths of 40 μm (Figures 1B). As evidenced by the energy-dispersive X-ray spectroscopy (EDX) element mapping images, each element (Ni and Ti) in the sample was distributed uniformly (Figures 1C and 1D). The atomic force microscopy (AFM) morphology (Figures 1E–1G) shows that the metal surfaces are exceptionally

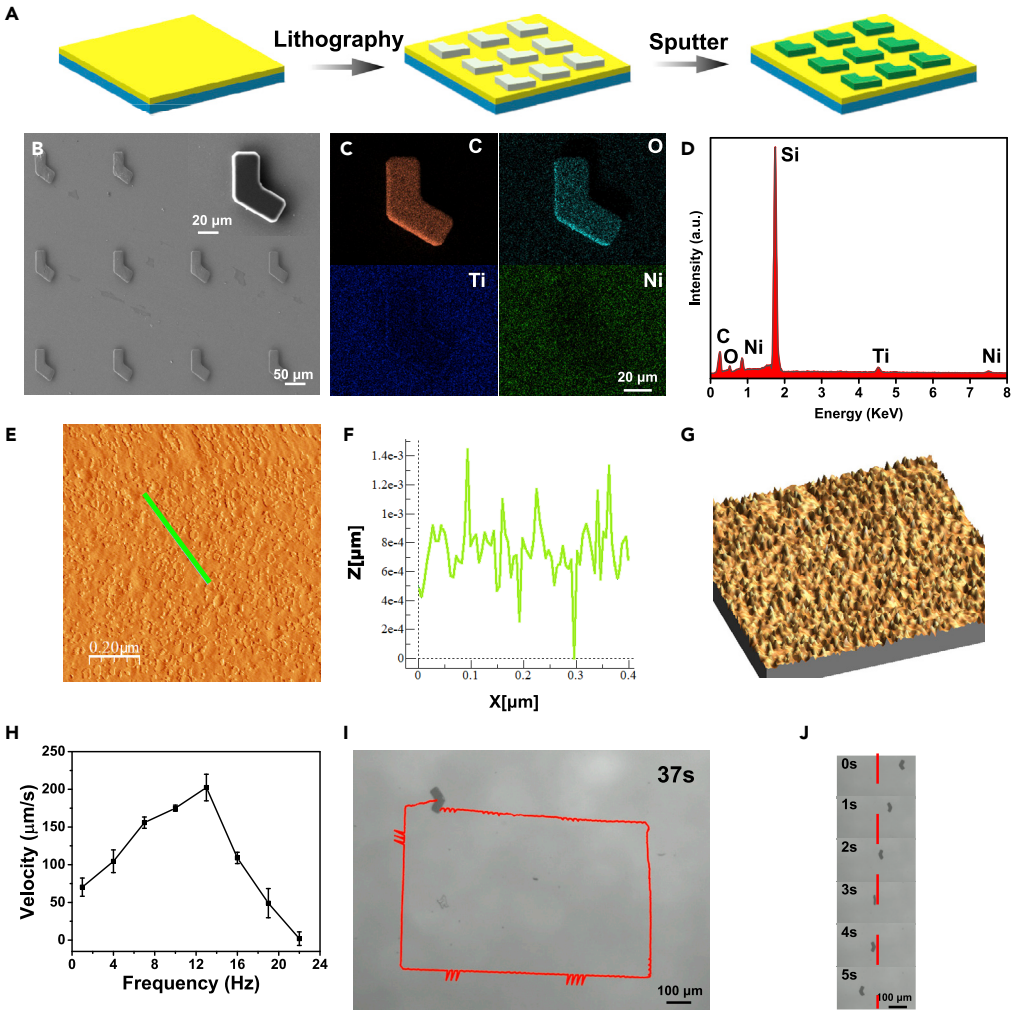

Figure 1. Fabrication and characterization of AMRs

(A) Illustration of the fabrication process for AMRs.

(B) SEM image of the AMRs. The inset is a zoomed-in image. Scale bars are 50 μm and 20 μm, respectively.

(C) EDX elemental mapping and (D) composition of AMRs. Scale bar is 20 μm.

(E) 2D AFM image and (F) surface profile. Scale bar is 0.2 μm.

(G) 3D AFM image.

(H) Velocity profile of AMRs as a function of rotational frequency. Error bars are ±SEM.

(I) Optical images were taken every 1 s of a microrobot moving at 5 Hz. The magnetic field strength was 10 mT and the frequency was 5 Hz. Scale bar is 100 μm.

(J) Motion control along the rectangle-shaped path. The trajectory (red line) was plotted using a MATLAB tracking algorithm. Scale bars on all images are 100 μm.

smooth with a root mean square (RMS) roughness (Rq) of 1 to 3 nm, indicating uniform and smooth surfaces at the nanoscale; this is consistent with SEM observations.

To test their magnetically actuated locomotion, AMRs were magnetically manipulated using a 10 mT rotating magnetic field generated by three orthogonal pairs of electromagnetic coils arranged in Helmholtz configuration[42]. The velocity of AMRs increased linearly with increasing rotating magnetic field frequency from 1 Hz to 13 Hz, as shown in Figures 1H. The average forward velocity of the AMRs at 13 Hz was measured to be 202.39 μms^{-1}. After reaching 13 Hz, a sharp decrease in velocity occurred due to step-out; this is consistent with previously reported step-out behaviors (Cheang et al., 2014a). To demonstrate their steerability, the AMRs were directed to move along a rectangle-shaped path. (Figures 1I and Video S1). A representative AMR moving in a straight under the actuation of a 10 mT rotating field at 5 Hz is shown in

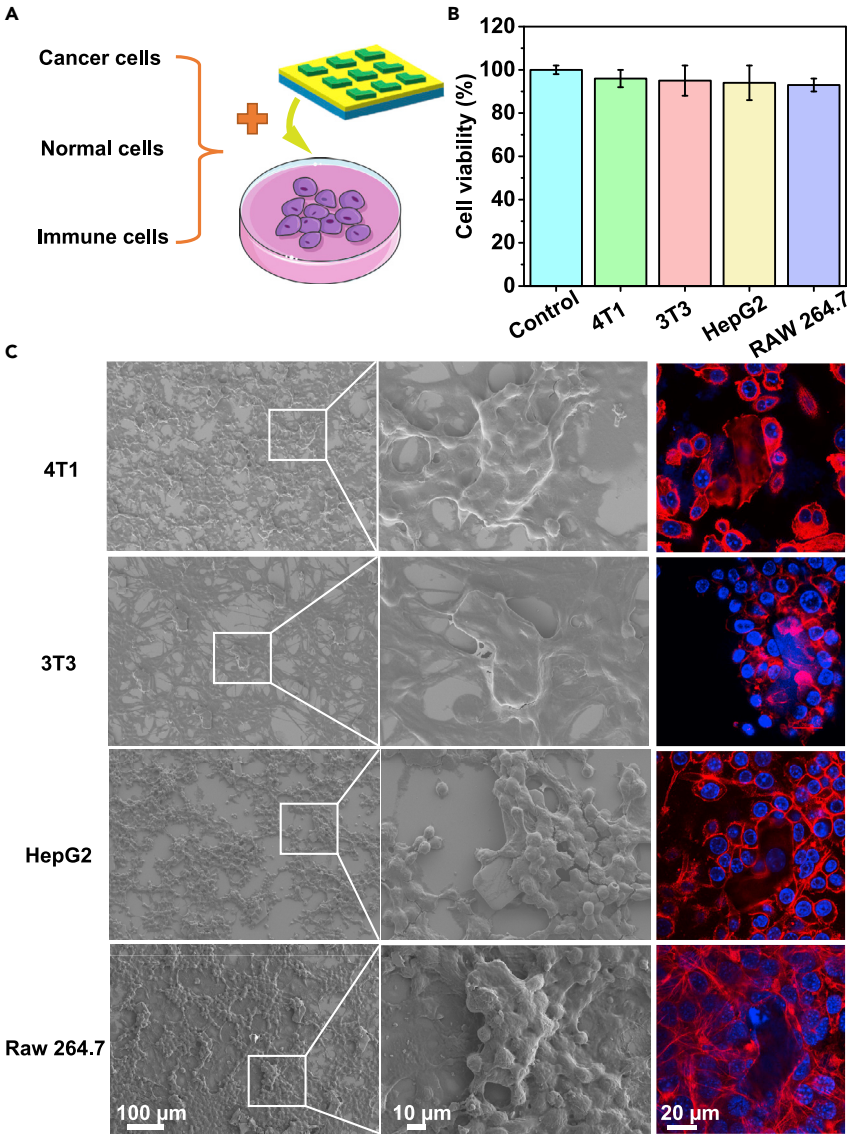

Figure 2. Cytotoxicity evaluation of AMRs

(A) Schematic diagram of cell culture with AMRs.

(B) Cell viability test by CCK-8 incubated with AMRs for 24 h. Error bars are ±SEM, P values were calculated by one-way ANOVA used to compare means. Asterisks indicate significant differences, *$p < 0.05$, $n = 3$.

(C) SEM and confocal images of different cells (4T1, 3T3, HepG2, and RAW 264.7) incubated with AMRs. Cell nuclei (blue) were stained with DAPI after 24 h, cytoskeletons were stained with TRITC-phalloidin (red). Left panel, scale bar, 100 μm; middle panel, scale bar, 10 μm and right panel, scale bar, 20 μm.

Figures 1J. The verification of control over speed and direction demonstrated the feasibility of controlling the AMRs for targeted biomedical applications.

Cytotoxicity evaluation of AMRs

To prove the cytocompatibility of the AMRs, their cellular cytotoxicity and cell adhesion were studied. A series of cell lines (cancer cells, fibroblasts, and macrophages) was used to gain a comprehensive evaluation of the biocompatibility of AMRs (Figure 2A). CCK-8 assay was carried out to test the cell viability of AMRs against mouse embryo fibroblast cells 3T3, mouse mammary cancer cell 4T1, human hepatoma cells line HepG2, and mouse macrophages RAW264.7. As shown in Figure 2B, all of the cells proliferated well on the AMRs and displayed no significant cytotoxicity after 24 h. Cell adhesion is also one of the important

indicators of cell activity on the AMRs. Cellular adhesion morphology was observed using scanning electron microscopy (SEM). The number of cells adhered to the AMRs was not significantly different between the four cell lines. Cell morphology was further examined after staining the cytoskeleton of the cell with TRITC-phalloidin (red), counterstained with DAPI (blue), and observed by the confocal microscope. Cells were well spread and distributed, as shown in Figure 2C.

Inducing M1 macrophage polarization by AMRs

It is well established that inducible nitric oxide synthase (iNOS), tumor necrosis factor-α (TNF-α), cluster of differentiation 86 (CD86), and interleukin-1 (IL-1) are defined as polarization markers of M1 macrophages and arginase-1 (Arg-1), transforming growth factor-β (TGF-β), mannose receptor C-type 1 (MRC1, also CD206), and interleukin-10 (IL-10) are defined as markers of M2 macrophages (Jin et al., 2019). Based on these markers, immunofluorescent staining, flow cytometry analysis, and real-time PCR were performed to characterize macrophage polarization induced by the AMRs. Immunofluorescent staining shows that the macrophages on the AMRs displayed a high expression of iNOS (M1 marker), whereas expression of Arg-1 (M2 marker) is very low, as shown in Figure 3A. Real-time PCR analysis proved that the macrophages had a higher expression level of M1-macrophage-related genes (IL-1 and TNF-α) and a lower level of M2-macrophage-related genes (IL-10 and TGF-β) on the AMRs (Figure 3B and 3C). M1 macrophage polarization was also verified by flow cytometry results. AMRs treatment showed significant expression of M1 biomarker (CD86) at approximately 90% (Figure 3D and 3E). These results strongly indicate that the macrophages were polarized to the M1 phenotype on the surfaces of the AMRs.

Drug loading on AMRs

Drug loading and release are critical functions for targeted tumor therapy using the AMRs. To load drug molecules on AMRs, the surface of the AMRs was modified by sodium citrate and allowed to bind to positively changed DOX molecules via electrostatic interactions. It has been reported that sodium citrate has plentiful active carboxyl groups, often used as stabilizers to modify Gold (Au), Ti, and magnetic nanoparticles for improved biocompatibility (Kang et al., 2018; Murphy and Jana, 2002; Raza et al., 2016). Figure 4A shows the schematic of the surface functionalization of AMRs. Zeta potential measurements were performed to characterize the charge of the surfaces of the AMRs before and after modification, the results are presented in Figure 4B. For the unmodified AMRs with Ti surfaces, the zeta potential was slightly negative (∼−5 mV) under PBS 7.4 conditions, which were consistent with previous reports (Miyauchi et al., 2004; Tsang et al., 2019). The citrate-modified AMRs have a negative surface charge with a zeta potential of -22.6 ± 4.9 mV. After being loaded with DOX, the zeta potentials of the AMRs increased to -10 ± 3.7 mV, indicating that the cationic DOX ions are adsorbed on the surfaces of the modified AMRs. DOX loading efficiency (DLE, defined as the weight ratio of DOX to the modified AMRs) was found to be 45%.

pH-responsive drug release

Considering the relatively acidic environments of tumor tissues compared with healthy tissues (Vaupel et al., 1989), it is possible to achieve pH-responsive drug release when the AMRs reach the tumor. To verify this, the drug release profiles for the DOX-loaded AMRs were characterized in PBS buffer at neutral pH 7.4 and acidic pH 5.5. As shown in Figure 4C, the drug release profile at neutral pH displayed a relatively slow-release profile; on the other hand, the drug release profile at pH 5.5 suggests a burst drug release of almost 45% within the first 12 h, then followed by a slow and sustained release. The initial and overall release rates of the whole test period were faster in acidic conditions than in neutral conditions. The maximum DOX release from the surface of the AMRs after 48 h at pH 5.5 and pH 7.4 was about 50% and 28%, respectively. The pH-sensitive behavior is due to the disruption of the electrostatic interaction (Curry et al., 2015). When pH is decreased, the $-NH_2$ group of DOX undergoes protonation, which could weaken the electrostatic interaction between DOX and AMRs, leading to a higher release. The pH-sensitive drug release mechanism can be exploited to minimize drug release near healthy tissue and reduce side effects during drug delivery.

Polarized macrophages and magnetic dual targeting cancer cell therapy

Conventional 2D tumor cell culture models cannot realistically reflect the situation of targeted tumor therapy *in vivo*. To simulate the complexity of the *in vivo* tumor environment, the antitumor efficacy of DOX-loaded microrobots was evaluated using a 3D tumor spheroids model (Figure 4D and 4E). Schematic of macrophage and magnetic dual-targeted cancer cell therapy was presented in Figure 4G. Multiple

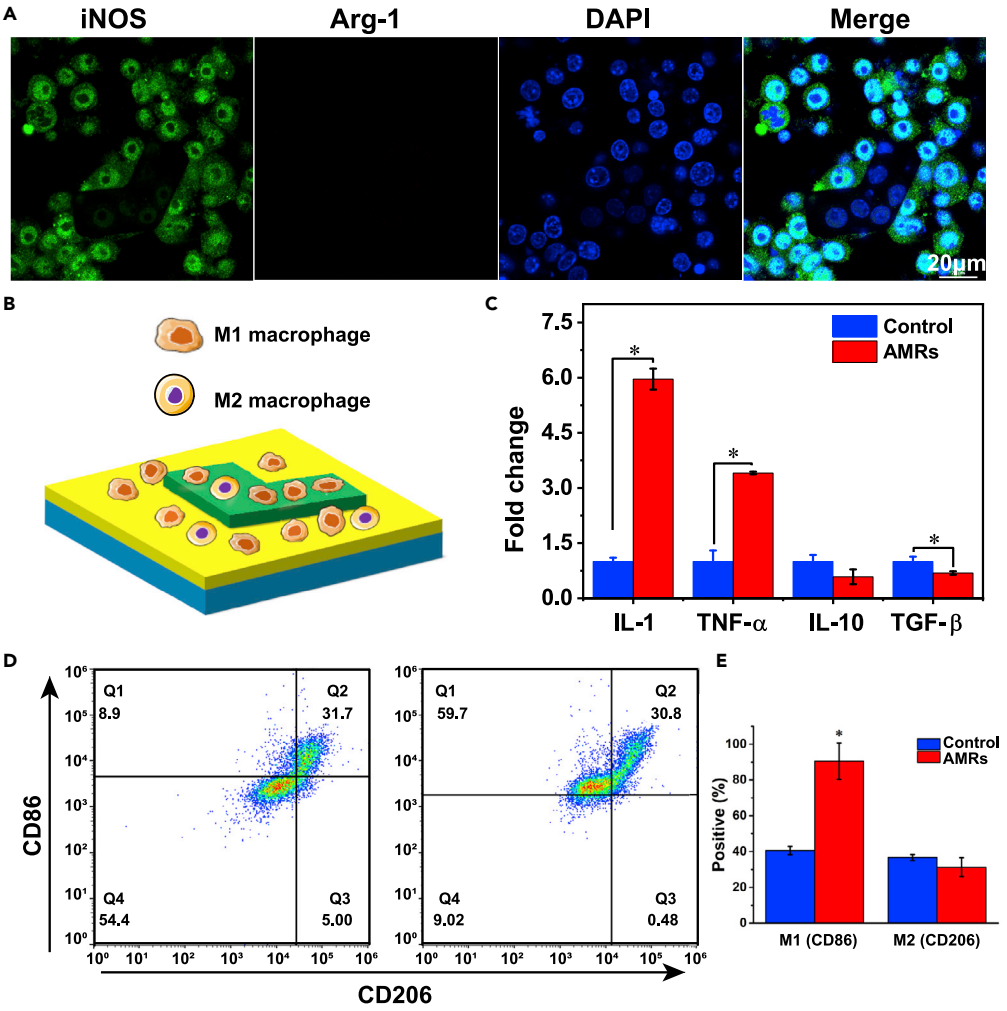

Figure 3. Polarization of M1 macrophages induced by AMRS

(A) Representative images of double immunofluorescence of iNOS antibody (green, M1 macrophage), Arg-1 (red, M2 macrophage), and nuclei (blue). Scale bar is 20 μm.

(B) Illustration of macrophages displaying different degrees of polarization cultured on the AMRs.

(C) Real-time PCR analysis of the RAW 264.7 cells cultured on the AMRs for 1 day, housekeeping gene β-actin was used as an internal control.

(D) Flow cytometric analysis of CD206 and CD86 after treatment with AMRs.

(E) Quantitative data of M1 CD86 and M2 CD206 population (%). Error bars are ±SEM. p values were calculated by one-way ANOVA, *$p < 0.05$.

AMRs loaded with DOX and M1 macrophages were actuated by a 10 mT rotating magnetic field at 10 Hz, as shown in a representative experiment in Figure 4F and Video S2. Driven by a rotating magnetic field, the AMRs moved toward the tumor spheroids from afar. After reaching the proximity of the tumor spheroids, the rotating magnetic field was turned off; this allowed the macrophages to achieve tumor-specific targeting of individual tumor spheroids. AMRs were incubated for 24 h and spheroids viability was tested using live/dead staining. In the control groups with no AMRs, only live cells (green) were observed with no dead cells (red) present, as shown in the representative case in Figure 4H. In the groups using AMRs with dual magnetic field and M1 macrophage targeting, dead cells were detected, demonstrating that the DOX released from dual targeting AMRs could kill tumor cells.

DISCUSSION

The ideal micro/nanorobots need to have accurate targeting and autonomous drug delivery ability, and at the same time, be stable and non-toxic in the biological environment and degradable after performing

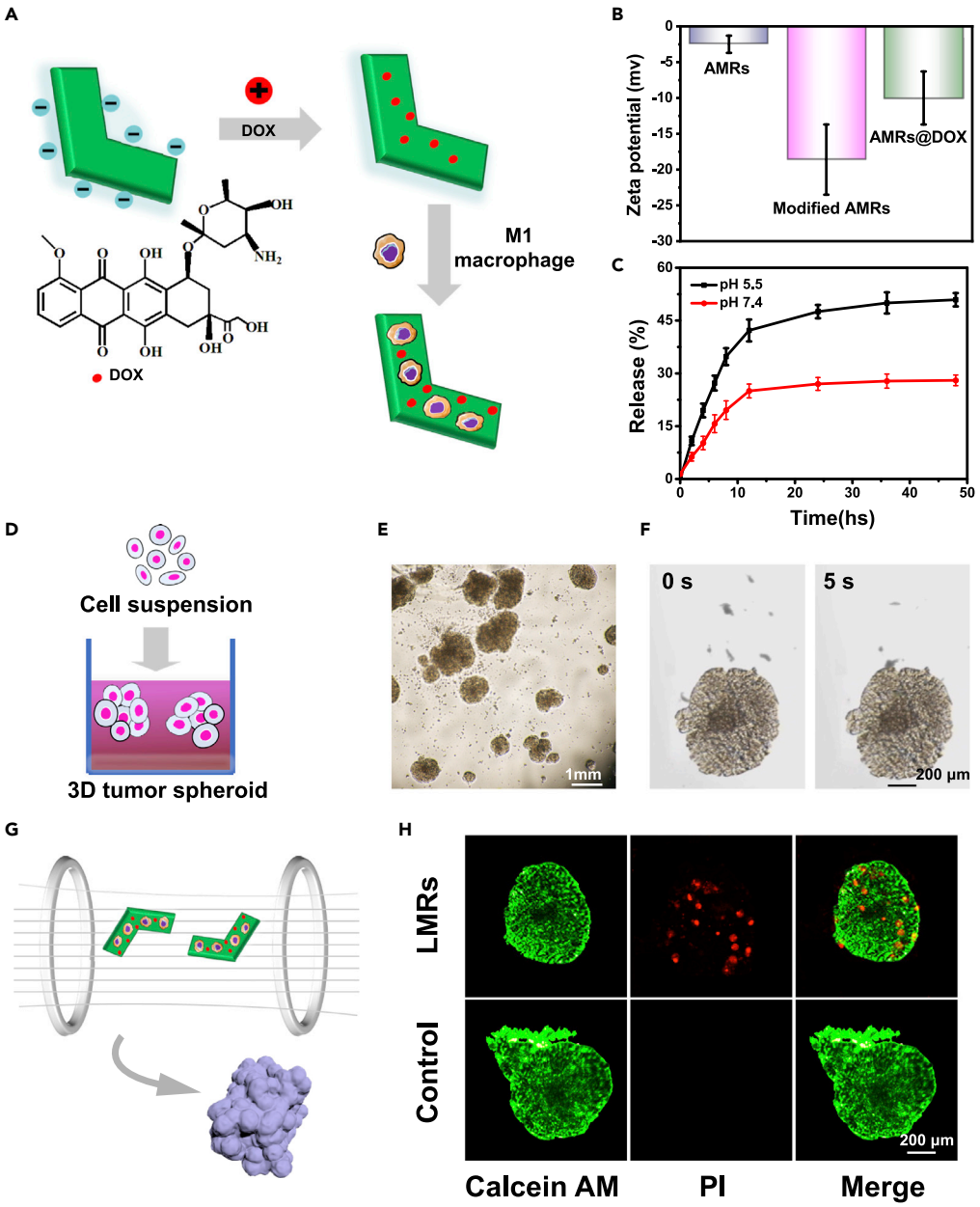

Figure 4. Polarized macrophages and magnetic dual targeting cancer cell therapy

(A) Schematic of functionalization and drug conjugation of AMRs.

(B) Zeta potentials of AMRs, modified AMRs, and DOX-loaded AMRs (DOX@AMRs).

(C) The cumulative drug release profile of DOX@AMRs at different pH.

(D) Schematic of tumor spheroid formation by culturing 4T1 tumor cells in matrigel and agarose.

(E) A representative photograph of tumor spheroids. Scale bar is 1 mm.

(F) Dual targeting of AMRs toward a tumor spheroid using magnetic guidance and M1 macrophage tumor-specific targeting. Scale bar is 200 μm.

(G) Schematic of macrophage and magnetic dual-targeted cancer cell therapy.

(H) Calcein-AM (green)/PI (red) assay was used to visualize the live cells (green) and dead cells (red) in the tumor spheroids. Error bars are ±SEM. Scale bar is 200 μm.

their tasks. Although micro/nanorobots have achieved encouraging results in tumor targeting, there are many problems and obstacles to be overcome before they can be used in clinical applications. In the past, relatively few designs of micro/nanorobots considered how the surface properties of the material

can be utilized to interact with cells to promote targeting capability. It is known that immune cells can differentiate into M1 or M2 phenotypes based on the properties of the surface they are cultured on, and the M1 and M2 phenotypes can inhibit and promote tumor development, respectively. Thus, using material-based modulation of macrophage polarization to design microrobots that are endowed with the tumor-specific targeting and inhibition capability of M1 macrophages is a promising strategy in cancer immunotherapy. In this work, we used the nano-smooth surfaces of drug-loaded magnetic microrobots to activate M1 macrophages for tumor spheroid targeting.

In summary, we developed a type of magnetic and M1 macrophage dual targeting drug-loaded microrobots with immunomodulatory capability for targeted cancer cell therapy, and we evaluated their targeted therapy performance *in vitro* experiments. The microrobots exhibited excellent biocompatibility against normal cells and immune cells. Electrostatic interactions between positively charged drug molecules and negatively charged microrobot surface promoted efficient drug loading and enabled pH-responsive drug release. Owing to their nano-smooth surfaces, the microrobots promoted M1 polarization of macrophages demonstrated by immunofluorescence, flow cytometry, and real-time PCR, which enhanced tumor-specific targeting and tumor growth inhibition toward 3D tumor spheroids. Combined with magnetic actuated motion, the microrobots can travel a long distance to the proximity of the tumor spheroids and then allow the M1 macrophages to specifically target individual spheroids. This study provides insights into the design and fabrication of medical microrobots and promotes the cross-disciplinary development of microrobots and targeted tumor therapy. By emphasizing the surface properties of the AMRs, insights were gained into how cellular behavior mechanisms can be exploited for targeted tumor therapy.

Limitations of the study

Future work to improve the capabilities of the microrobots will focus on several aspects: biodegradability, drug loading efficiency, imaging, *in vivo* experiments, and molecular mechanisms for phenotype activation. The material used to fabricate the microrobots was SU-8, which is not biodegradable. We will try to fabricate the microrobots using biodegradable hydrogel and iron oxide nanoparticles. Once the hydrogel is degraded, the drug within and the macrophages will be released at the tumor site, and the nanoparticles will be cleared by the body. While this work was able to achieve triggered release under acidic conditions using the loading method of non-covalent electrostatic adsorption, it is important to increase the loading efficiency of the microrobots for practical applications. A higher concentration of anticancer drugs internalized into the cancer cells can yield a better therapeutic result; thus, we will continue to investigate ways to increase drug loading efficiency while maintaining release behaviors favorable to cancer therapy. Biocompatible porous materials (such as metal-organic frameworks and porous bioactive titanium) and stimuli-responsive polymers can be integrated with micro/nanorobots for the enhancement of drug loading capability in the future work.

The microrobots will also be further modified to be used with photoacoustic (PA) imaging by incorporating materials that can produce high contrast such as gold or black phosphorus. This work evaluated the dual targeting ability of AMRs against tumor spheroids, which is sufficient for proof of concept; to evaluate the *in vivo* efficacy for practical applications, future work will include targeted therapy evaluation in mouse and zebrafish cancer models. While the results conclusively showed that the surface properties of the microrobots can consistently activate the M1 phenotype, we plan to conduct further experiments in the future to gain a deeper insight into the molecular mechanisms that lead phenotype activity by priming control groups, such as RAW 264.7 macrophages, into the M1 or M2 phenotypes using LPS/IFN-γ and IL-4-inducing agent respectively,. Previous work also revealed that rough dioxide microparticles cannot activate the immune response, while spiky microparticles can exert mechanical force and trigger NLRP3 inflammasome activation (Wang et al., 2018). This not only supports our results but also suggests that integrating spiky structures into the designs of future micro/nanorobots might be beneficial to their immunomodulatory function.

STAR★METHODS

Detailed methods are provided in the online version of this paper and include the following:

- KEY RESOURCES TABLE
- RESOURCE AVAILABILITY

SUPPLEMENTAL INFORMATION

Supplemental information can be found online at https://doi.org/10.1016/j.isci.2022.104507.

ACKNOWLEDGMENTS

We acknowledge the support from the Department of Education of Guangdong (2021ZDZX2037), Science and Technology Innovation Committee Foundation of Shenzhen (20200925155648005, RCYX20210609103644015, and ZDSYS20200811143601004), Shenzhen municipal government (Peacock Plan, 20181119590C). The authors would like to acknowledge the technical support from the SUSTech Core Research Facilities (SCRF).

AUTHOR CONTRIBUTIONS

X.S. conceived the ideas, prepared the manuscript, and performed most of the experiments. W.F. helped performed the main part of the magnetic control experiment. U.K.C. procured funding, supervised the project, reviewed the manuscript, and finalized the manuscript.

DECLARATION OF INTERESTS

The authors declare no competing interests.

Received: November 11, 2021
Revised: April 4, 2022
Accepted: May 27, 2022
Published: July 15, 2022

REFERENCES

Agrahari, V., Agrahari, V., Chou, M.L., Chew, C.H., Noll, J., and Burnouf, T. (2020). Intelligent micro-/nanorobots as drug and cell carrier devices for biomedical therapeutic advancement: promising development opportunities and translational challenges. Biomaterials *260*, 120163.

Alapan, Y., Bozuyuk, U., Erkoc, P., Karacakol, A.C., and Sitti, M. (2020). Multifunctional surface microrollers for targeted cargo delivery in physiological blood flow. Sci. Robot *5*, eaba5726. https://doi.org/10.1126/scirobotics.aba5726.

Esteban-Fernández de Ávila, B., Gao, W.W., Karshalev, E., Zhang, L.F., and Wang, J. (2018). Cell-like micromotors. Accounts Chem. Res. *51*, 1901–1910. https://doi.org/10.1021/acs.accounts.8b00202.

Buss, N., Yasa, O., Alapan, Y., Akolpoglu, M.B., and Sitti, M. (2020). Nanoerythrosome-functionalized biohybrid microswimmers. APL Bioeng. *4*, 026103. https://doi.org/10.1063/1.5130670.

Cheang, U.K., Kim, H., Milutinović, D., Choi, J., and Kim, M.J. (2017). Feedback control of an achiral robotic microswimmer. J. Bionic. Eng. *14*, 245–259. https://doi.org/10.1016/s1672-6529(16)60395-5.

Cheang, U.K., Meshkati, F., Kim, D., Kim, M.J., and Fu, H.C. (2014a). Minimal geometric requirements for micropropulsion via magnetic rotation. Phys. Rev. E Stat. Nonlin Soft. Matter Phys. *90*, 033007. https://doi.org/10.1103/physreve.90.033007.

Cheang, U.K., Meshkati, F., Kim, D., Kim, M.J., and Fu, H.C. (2014b). Minimal geometric requirements for micropropulsion via magnetic rotation. Phys. Rev. E. *90*, 033007. https://doi.org/10.1103/physreve.90.033007.

Cohen, K.J., Rubinstein, B.Y., Kenneth, O., and Leshansky, A.M. (2019). Unidirectional propulsion of planar magnetic nanomachines. Phys. Rev. Appl. *12*, 014025. https://doi.org/10.1103/physrevapplied.12.014025.

Curry, D., Cameron, A., MacDonald, B., Nganou, C., Scheller, H., Marsh, J., Beale, S., Lu, M.S., Shan, Z., Kaliaperumal, R., et al. (2015). Adsorption of doxorubicin on citrate-capped gold nanoparticles: insights into engineering potent chemotherapeutic delivery systems. Nanoscale *7*, 19611–19619. https://doi.org/10.1039/c5nr05826k.

Deng, C.F., Zhang, Q., Jia, M.D., Zhao, J., Sun, X., Gong, T., and Zhang, Z.R. (2019). Tumors and their microenvironment dual-targeting chemotherapy with local immune adjuvant therapy for effective antitumor immunity against breast cancer. Adv. Sci. *6*, 1801868. https://doi.org/10.1002/advs.201801868.

Duan, Z.J., and Luo, Y.P. (2021). Targeting macrophages in cancer immunotherapy. Signal Transduct. Tar. *6*, 127. https://doi.org/10.1038/s41392-021-00506-6.

Ebrahimi, N., Bi, C.H., Cappelleri, D.J., Ciuti, G., Conn, A.T., Faivre, D., Habibi, N., Hošovský, A., Hosovsky, A., Iacovacci, V., et al. (2021). Magnetic actuation methods in bio/soft robotics. Adv. Funct. Mater. *31*, 2005137. https://doi.org/10.1002/adfm.202005137.

Fan, Z., Zhu, P., Zhu, Y., Wu, K., Li, C.Y., and Cheng, H. (2020). Engineering long-circulating nanomaterial delivery systems. Curr. Opin. Biotechnol. *66*, 131–139. https://doi.org/10.1016/j.copbio.2020.07.006.

Felfoul, O., Mohammadi, M., Taherkhani, S., de Lanauze, D., Zhong Xu, Y., Loghin, D., Essa, S., Jancik, S., Houle, D., Lafleur, M., et al. (2016). Magneto-aerotactic bacteria deliver drug-containing nanoliposomes to tumour hypoxic regions. Nat. Nanotechnol. *11*, 941–947. https://doi.org/10.1038/nnano.2016.137.

Gao, C.Y., Lin, Z.H., Wang, D.L., Wu, Z.G., Xie, H., and He, Q. (2019). Red blood cell-mimicking micromotor for active photodynamic cancer therapy. Acs Appl. Mater. Inter. *11*, 23392–23400. https://doi.org/10.1021/acsami.9b07979.

Han, J., Zhen, J., Du Nguyen, V., Go, G., Choi, Y., Ko, S.Y., Park, J.O., and Park, S. (2016). Hybrid-actuating macrophage-based microrobots for active cancer therapy. Sci. Rep-Uk *6*, 28717. https://doi.org/10.1038/srep28717.

Han, X., Wang, R., Xu, J., Chen, Q., Liang, C., Chen, J., Zhao, J., Chu, J., Fan, Q., Archibong, E., et al. (2019). In situ thermal ablation of tumors in combination with nano-adjuvant and immune checkpoint blockade to inhibit cancer metastasis and recurrence. Biomaterials *224*, 119490. https://doi.org/10.1016/j.biomaterials.2019.119490.

Hotchkiss, K.M., Reddy, G.B., Hyzy, S.L., Schwartz, Z., Boyan, B.D., and Olivares-Navarrete, R. (2016). Titanium surface characteristics, including topography and wettability, alter macrophage activation. Acta Biomater. *31*, 425–434. https://doi.org/10.1016/j.actbio.2015.12.003.

Hu, W., Liu, C., Bi, Z.Y., Zhou, Q., Zhang, H., Li, L.L., Zhang, J., Zhu, W., Song, Y.Y.Y., Zhang, F., et al. (2020). Comprehensive landscape of extracellular vesicle-derived RNAs in cancer initiation, progression, metastasis and cancer immunology. Mol. Cancer *19*, 102. https://doi.org/10.1186/s12943-020-01199-1.

Huo, M.F., Wang, L.Y., Zhang, L.L., Wei, C.Y., Chen, Y., and Shi, J.L. (2020). Photosynthetic tumor oxygenation by photosensitizer-containing cyanobacteria for enhanced photodynamic therapy. Angew Chem. Int. Edit *132*, 1922–1929. https://doi.org/10.1002/ange.201912824.

Jin, S.S., He, D.Q., Luo, D., Wang, Y., Yu, M., Guan, B., Fu, Y., Li, Z.X., Zhang, T., Zhou, Y.H., et al. (2019). A biomimetic hierarchical nanointerface orchestrates macrophage polarization and mesenchymal stem cell recruitment to promote endogenous bone regeneration. ACS Nano *13*, 6581–6595. https://doi.org/10.1021/acsnano.9b00489.

Kang, H., Jung, H.J., Kim, S.K., Wong, D.S.H., Lin, S., Li, G., Dravid, V.P., and Bian, L.M. (2018). Magnetic manipulation of reversible nanocaging controls *in vivo* adhesion and polarization of macrophages. ACS Nano *12*, 5978–5994. https://doi.org/10.1021/acsnano.8b02226.

Ladányi, A. (2015). Prognostic and predictive significance of immune cells infiltrating cutaneous melanoma. Pigment Cell Melanoma Res. *28*, 490–500. https://doi.org/10.1111/pcmr.12371.

Luedde, T., Beraza, N., Kotsikoris, V., van Loo, G., Nenci, A., De Vos, R., Roskams, T., Trautwein, C., and Pasparakis, M. (2007). Deletion of NEMO/IKKγ in liver parenchymal cells causes steatohepatitis and hepatocellular carcinoma. Cancer Cell *11*, 119–132. https://doi.org/10.1016/j.ccr.2006.12.016.

Magdanz, V., Khalil, I.S.M., Simmchen, J., Furtado, G.P., Mohanty, S., Gebauer, J., Xu, H.F., Klingner, A., Aziz, A., Medina-Sánchez, M., et al. (2020). IRONSperm: sperm-templated soft magnetic microrobots. Sci. Adv. *6*, eaba5855. https://doi.org/10.1126/sciadv.aba5855.

McWhorter, F.Y., Wang, T., Nguyen, P., Chung, T., and Liu, W.F. (2013). Modulation of macrophage phenotype by cell shape. Proc. Natl. Acad. Sci. U S A. *110*, 17253–17258. https://doi.org/10.1073/pnas.1308887110.

Mirzae, Y., Dubrovski, O., Kenneth, O., Morozov, K.I., and Leshansky, A.M. (2018). Geometric constraints and optimization in externally driven propulsion. Sci. Robot *3*, aas8713. https://doi.org/10.1126/scirobotics.aas8713.

Miskin, M.Z., Cortese, A.J., Dorsey, K., Esposito, E.P., Reynolds, M.F., Liu, Q.K., Cao, M.C., Muller, D.A., McEuen, P.L., and Cohen, I. (2020). Electronically integrated, mass-manufactured, microscopic robots. Nature *584*, 557–561. https://doi.org/10.1038/s41586-020-2626-9.

Miyauchi, M., Ikezawa, A., Tobimatsu, H., Irie, H., and Hashimoto, K. (2004). Zeta potential and photocatalytic activity of nitrogen doped TiO2 thin films. Phys. Chem. Chem. Phys. *6*, 865. https://doi.org/10.1039/b314692h.

Murphy, C.J., and Jana, N.R. (2002). Controlling the aspect ratio of inorganic nanorods and nanowires. Adv. Mater *14*, 80–82. https://doi.org/10.1002/1521-4095(20020104)14:1<80::aid-adma80>3.0.co;2-#.

Nikitin, M.P., Zelepukin, I.V., Shipunova, V.O., Sokolov, I.L., Deyev, S.M., and Nikitin, P.I. (2020). Enhancement of the blood-circulation time and performance of nanomedicines via the forced clearance of erythrocytes. Nat. Biomed. Eng. *4*, 717–731. https://doi.org/10.1038/s41551-020-0581-2.

Raza, G., Amjad, M., Kaur, I., Baalousha, M., Lead, J., and Wen, D.S. (2016). Stability and aggregation kinetics of titania nanomaterials under environmentally realistic conditions. Environ. Sci. Technol. *50*, 12525. https://doi.org/10.1021/acs.est.6b05148.

Sahu, A., Kwon, I., and Tae, G. (2020). Improving cancer therapy through the nanomaterials-assisted alleviation of hypoxia. Biomaterials *228*, 119578. https://doi.org/10.1016/j.biomaterials.2019.119578.

Schmidt, C.K., Medina-Sánchez, M., Edmondson, R.J., and Schmidt, O.G. (2020). Engineering microrobots for targeted cancer therapies from a medical perspective. Nat. Commun. *11*, 5618. https://doi.org/10.1038/s41467-020-19322-7.

Song, X.X., Liu, F.W., Qiu, C.J., Coy, E., Liu, H., Aperador, W., Załęski, K., Zaleski, K., Li, J.J., Song, W., et al. (2021). Nanosurfacing Ti alloy by weak alkalinity-activated solid-state dewetting (AAD) and its biointerfacial enhancement effect. Mater. Horiz. *8*, 912–924. https://doi.org/10.1039/d0mh01837f.

Soto, F., Wang, J., Ahmed, R., and Demirci, U. (2020). Medical micro/nanorobots in precision medicine. Adv. Sci. *7*, 2002203. https://doi.org/10.1002/advs.202002203.

Tsang, C.H.A., Li, K., Zeng, Y.X., Zhao, W., Zhang, T., Zhan, Y.J., Xie, R.J., Leung, D.Y.C., and Huang, H.B. (2019). Titanium oxide based photocatalytic materials development and their role of in the air pollutants degradation: overview and forecast. Environ. Int. *125*, 200–228. https://doi.org/10.1016/j.envint.2019.01.015.

Vaupel, P., Kallinowski, F., and Okunieff, P. (1989). Blood flow, oxygen and nutrient supply, and metabolic microenvironment of human tumors: a review. Cancer Res. *49*, 6449–6465.

Wang, B., Kostarelos, K., Nelson, B.J., and Zhang, L. (2021). Trends in micro-/nanorobotics: materials development, actuation, localization, and system integration for biomedical applications. Adv. Mater *33*, 2002047. https://doi.org/10.1002/adma.202002047.

Wang, J., Chen, H.J., Hang, T., Yu, Y., Liu, G.S., He, G., Xiao, S., Yang, B.R., Yang, C.D., Liu, F.M., et al. (2018). Physical activation of innate immunity by spiky particles. Nat. Nanotechnol. *13*, 1078–1086. https://doi.org/10.1038/s41565-018-0274-0.

Wang, J., Zhu, R.R., Gao, B., Wu, B., Li, K., Sun, X.Y., Liu, H., and Wang, S.L. (2014). The enhanced immune response of hepatitis B virus DNA vaccine using SiO2@LDH nanoparticles as an adjuvant. Biomaterials *35*, 466–478. https://doi.org/10.1016/j.biomaterials.2013.09.060.

Waterfield, J.D., Ali, T.A., Nahid, F., Kusano, K., and Brunette, D.M. (2010). The effect of surface topography on early NFkB signaling in macrophages. J. Biomed Mater Res. A *95*, 837–847. https://doi.org/10.1002/jbm.a.32857.

Woo, S.R., Corrales, L., and Gajewski, T.F. (2015). Innate immune recognition of cancer. Annu. Rev. Immunol. *33*, 445–474. https://doi.org/10.1146/annurev-immunol-032414-112043.

Wu, Z., Esteban-Fernández de Ávila, B., Martín, A., Christianson, C., Gao, W.W., Thamphiwatana, S.K., Escarpa, A., He, Q., Zhang, L.F., and Wang, J. (2015). RBC micromotors carrying multiple cargos towards potential theranostic applications. Nanoscale *7*, 13680–13686. https://doi.org/10.1039/c5nr03730a.

Wu, Z.G., Chen, Y., Mukasa, D., Pak, O.S., and Gao, W. (2020). Medical micro/nanorobots in complex media. Chem. Soc. Rev. *49*, 8088–8112. https://doi.org/10.1039/d0cs00309c.

Wu, Z.G., Li, T.L., Li, J.X., Gao, W., Xu, T.L., Christianson, C., Gao, W.W., Galarnyk, M., He, Q.,

Zhang, L.F., and Wang, J. (2014). Turning erythrocytes into functional micromotors. ACS Nano *8*, 12041–12048. https://doi.org/10.1021/nn506200x.

Xia, Y., Rao, L., Yao, H., Wang, Z., Ning, P., and Chen, X. (2020). Engineering macrophages for cancer immunotherapy and drug delivery. Adv. Mater *32*, e2002054. https://doi.org/10.1002/adma.202002054.

Xu, H., Medina-Sánchez, M., Zhang, W., Seaton, M.P.H., Brison, D.R., Edmondson, R.J., Taylor, S.S., Nelson, L., Zeng, K., Bagley, S., et al. (2020a). Human spermbots for patient-representative 3D ovarian cancer cell treatment. Nanoscale *12*, 20467–20481. https://doi.org/10.1039/d0nr04488a.

Xu, H.F., Medina-Sanchez, M., and Schmidt, O.G. (2020b). Magnetic micromotors for multiple motile sperm cells capture, transport, and enzymatic release. Angew Chem. Int. Edit *132*, 15139–15147. https://doi.org/10.1002/ange.202005657.

Xu, H.F., Medina-Sánchez, M., Medina-Sanchez, M., Magdanz, V., Schwarz, L., Hebenstreit, F., and Schmidt, O.G. (2018). Sperm-hybrid micromotor for targeted drug delivery. ACS Nano *12*, 327–337. https://doi.org/10.1021/acsnano.7b06398.

Yan, X.H., Xu, J.B., Zhou, Q., Jin, D.D., Vong, C.I., Vong, C.A., Feng, Q., Ng, D.H.L., Bian, L., and Zhang, L. (2019). Molecular cargo delivery using multicellular magnetic microswimmers. Appl. Mater. Today *15*, 242–251. https://doi.org/10.1016/j.apmt.2019.02.006.

Yan, X.H., Zhou, Q., Vincent, M., Deng, Y., Yu, J.F., Xu, J.B., Xu, T.T., Tang, T., Bian, L.M., Wang, Y.X.J., et al. (2017). Multifunctional biohybrid magnetite microrobots for imaging-guided therapy. Sci. Robot *2*, eaaq1155. https://doi.org/10.1126/scirobotics.aaq1155.

Yong, S.B., Chung, J.Y., Song, Y., Kim, J., Ra, S., and Kim, Y.H. (2019). Non-viral nano-immunotherapeutics targeting tumor microenvironmental immune cells. Biomaterials *219*, 119401.

Zhai, Y., Su, J., Ran, W., Zhang, P., Yin, Q., Zhang, Z., Yu, H., and Li, Y. (2017). Preparation and application of cell membrane-camouflaged nanoparticles for cancer therapy. Theranostics *7*, 2575–2592. https://doi.org/10.7150/thno.20118.

Zhang, J., Shen, L.M., Li, X., Song, W.T., Liu, Y., and Huang, L. (2019). Nanoformulated codelivery of quercetin and alantolactone promotes an antitumor response through synergistic immunogenic cell death for microsatellite-stable colorectal cancer. ACS Nano *13*, 12511–12524. https://doi.org/10.1021/acsnano.9b02875.

Zhang, L., Zhao, Z.J., Wang, T., and Gong, J.L. (2018). Nano-designed semiconductors for electro- and photoelectro-catalytic conversion of carbon dioxide. Chem. Soc. Rev. *47*, 5423–5443. https://doi.org/10.1039/c8cs00016f.

Zhong, D.N., Li, W.L., Qi, Y.C., He, J., and Zhou, M. (2020). Photosynthetic biohybrid nanoswimmers: photosynthetic biohybrid nanoswimmers system to alleviate tumor hypoxia for FL/PA/MR imaging-guided enhanced radio--photodynamic synergetic therapy. Adv. Funct. Mater. *30*, 1910395. https://doi.org/10.1002/adfm.202070110.

Zhou, H., Mayorga-Martinez, C.C., Pané, S., Zhang, L., and Pumera, M. (2021). Magnetically driven micro and nanorobots. Chem. Rev. *121*, 4999–5041. https://doi.org/10.1021/acs.chemrev.0c01234.

STAR★METHODS

KEY RESOURCES TABLE

REAGENT or RESOURCE	SOURCE	IDENTIFIER
Antibodies		
TRITC-conjugated secondary antibody	Invitrogen	Cat#T-2769; RRID: AB_2556777
FITC-conjugated secondary antibody	Invitrogen	Cat#A21042; RRID: AB_141357
iNOs	Santa Cruz Biotechnology	Cat# sc-7271, RRID: AB_627810
Arg-1	Affinity Biosciences	Cat# DF6657, RRID: AB_2838619
CD86	eBioscience	Cat# 11-0860-85, RRID: AB_465146
CD206	eBioscience	Cat# 17-2061-82, RRID: AB_2637420
Chemicals, peptides, and recombinant proteins		
Bovine serum albumin (BSA)	Sigma Aldrich	Cat#A5378
Dextran	Sigma Aldrich	Cat#FD70S
Trizol	TaKaRa	Cat#9108
DAPI reagent	Solarbio	Cat#C0065
anti-fluorescence-attenuating sealer	Solarbio	Cat#S2100
Dulbecco's modified Eagle's medium (DMEM)	BI	Cat#06-1055-57-1A
Trypsin Protease	BI	Cat# 356234
Fetal bovine serum (FBS)	BI	Cat#04-010-1B
DOX	Sigma Aldrich	Cat#D1515
Matrigel	BD Biosciences	Cat# 356234
4% paraformaldehyde	Solarbio	Cat#P1110
Polydimethylsiloxane (Dow SYLGARD™ 184)	Dow Corning	Cat# 1673921
SU-8 developer	MicroChem	Cat#Y020100
SU-8 2015	MicroChem	Cat#YB0058
Critical commercial assays		
Cell counting kit-8 (CCK-8)	Dojindo	Cat#CK04
Calcein-AM/PI Double Stain Kit	Biyuntian	Cat#C2015S
SYBR® Green PCR Master Mix	TaKaRa	Cat#RR420A
PrimeScript RT reagent Kit	TaKaRa	Cat#RR037A
Experimental models: Cell lines		
4T1	Cell Bank of the Chinese Academic of Sciences	SCSP-5056
NIH-3T3	Cell Bank of the Chinese Academic of Sciences	SCSP-515
RAW 264.7	Cell Bank of the Chinese Academic of Sciences	SCSP-5036
HepG2	Cell Bank of the Chinese Academic of Sciences	SCSP-510
Oligonucleotides		
Primers for IL-1 Forward: AACCTGCTGGTGTGTGACGTTC	This paper	N/A
Primers for IL-1 Reverse: CAGCACGAGGCTTTTTTGTTGT	This paper	N/A
Primers for TNF-α Forward: CCTGTAGCCCACGTCGTAG	This paper	N/A
Primers for TNF-α Reverse: GGGAGTAGACAAGGTACAACCC	This paper	N/A

(*Continued on next page*)

Continued

REAGENT or RESOURCE	SOURCE	IDENTIFIER
Primers for IL-10 Forward: AGCCTTATCGGAAATGATCCAGT	This paper	N/A
Primers for IL-10 Reverse: GGCCTTGTAGACACCTTGGT	This paper	N/A
Primers for TGF-β Forward: ATATCTGCCATAACCGCACTG	This paper	N/A
Primers for TGF-β Reverse: CTGAAATGAAAGGGCGATCTAGT	This paper	N/A
Primers for β-actin Forward: GGCAGTGTTTTGGGCATATTC	This paper	N/A
Primers for β-actin Reverse: GATGACGATATCGCTGCGCTG	This paper	N/A
Software and algorithms		
Origin	OriginLab Corporation	https://www.originlab.com/
FlowJo software c10	Flowjo	https://www.flowjo.com/solutions/flowjo

RESOURCE AVAILABILITY

Lead contact

Further information and requests for resources and reagents should be directed to and will be fulfilled by the lead contact U Kei Cheang (cheanguk@sustech.edu.cn).

Materials availability

This study did not generate new unique reagents.

Data and code availability

The article includes all datasets generated or analyzed during this study. This paper does not report original code. Any additional information required to reanalyze the data reported in this paper is available from the lead contact upon request.

EXPERIMENTAL MODEL AND SUBJECT DETAILS

Cell lines and cell culture

4T1 mouse breast cancer cells (SCSP-5056), NIH-3T3 fibroblasts (SCSP-515), RAW 264.7 macrophages (SCSP-5036), and HepG2 liver cancer cells (SCSP-510) were obtained from the Cell Bank of the Chinese Academy of Sciences (Shanghai, China). Cells were cultured in DMEM supplemented with 10% (v/v) FBS and 1% (v/v) penicillin-streptomycin at 37°C in an atmosphere with 5% CO_2. All incubations were performed in DMEM at 37 °C. At 70–80% confluency, cells were trypsinized and subcultured for other experiments.

METHOD DETAILS

Fabrication of AMRs

The magnetic achiral microrobots were fabricated using standard photolithography and magnetron sputtering. First, dextran solution (10% w/v) was spin-coated on a clean silicon wafer at 1000 rpm for 10 s, followed by drying by baking at 120°C for 2 min to form a water-soluble sacrificial layer. Next, the SU-8 negative photoresist was spin-coated at 3,000 rpm, followed by soft-baking at 95°C for 2 min. Then the patterns with the shape of the AMRs were transferred from a chromium mask onto the SU-8 layer by UV exposure (SUSS MA6/BA6) for 20 s to induce photoresist cross-linking. After post-baking at 95°C for 2 min, development for 1 min, and dried at room temperature, well-defined achiral-shaped SU-8 microstructures were created. Subsequently, Ni and Ti metal layers were sequentially deposited onto the SU-8 microstructures via magnetron sputtering (KYKY-500CK-500ZF), with thicknesses of 300 nm and 30 nm, respectively; after this process, the AMRs with the composition of SU-8/Ni/Ti were created on

top of the sacrificial layer. Finally, the substrate with the AMRs is immersed in deionized water to dissolve the dextran sacrificial layer to release the AMRs for experiments.

Characterization of AMRs

The structures of the AMRs were confirmed using a scanning electron microscope (SEM, Zeiss Merlin, Germany) equipped with an energy dispersive spectrometry (EDS) analyzer at 200 kV. The element analysis was carried out using EDS. The surface roughness was examined using an atomic force microscope (AFM, MFP-3D Stand Alone, Asylum Research, USA). For AFM imaging, contact mode using oxide-sharpened silicon nitride tips was applied, and information was collected in an area of 1 × 1 μm.

The surface zeta potential was measured using a Malvern model Zetasizer Nano ZSP zeta potential analyzer (BI-200SM, Bruker, USA). Infrared spectra were obtained using a Fourier transform Spectrophotometer (Perkinelmer 1720 IR. USA) in potassium bromide disks.

Cell viability evaluation

Cell viability was assessed using CCK-8 kit according to the manufacturer's instructions. Briefly, 100 μL cell suspension was seeded in 96-well plates at a density of 2×10^4 cells per mL. AMRs were added to the cells and incubated overnight. Then, the CCK-8 reagent was added and incubated in the darkness for 1 h. Finally, the absorption value at 450 nm was read by a multifunctional full wavelength microplate reader (Infinite 200 Pro, Tecan Austria GmbH, Austria).

Immunofluorescent staining of polarized macrophages

The immune response of macrophages induced by the surface properties of the AMRs was verified using immunofluorescence staining of the polarized macrophages. In brief, murine macrophage cell line (RAW 264.7) was seeded onto the AMRs and cultured for 1 day. Then, the cells were fixed in 4% (w/v) paraformaldehyde for 15 min and washed with PBS three times. The fixed cells were permeabilized for 10 min in 0.1% Triton X-100 in PBS at 4°C. Next, the cells were blocked with 1 wt% BSA at RT for 1 h. Afterward, the cells were incubated with primary antibody diluted in blocking buffer (M1 marker, iNOS, 1:100; M2 marker, arg-1, 1:100) at 4°C for overnight. The next day, the cells were washed three times with PBS. After washing, the corresponding diluted secondary antibodies (TRITC Conjugated AffiniPure Goat Anti-Mouse IgG (H + L) and DyLight 488 Conjugated AffiniPure Donkey Anti-Rabbit IgG (H + L)) were added and incubated for 1 h, followed by washed with PBS three times. Finally, nuclei were counter-stained with DAPI for 5 min. The cells were washed again with PBS followed by the addition of the antifade mounting medium. The stained cells were imaged by confocal microscopy. The fluorescence intensity was quantitatively analyzed using flow cytometry (FACSVerse, BD, USA) with 10,000 events collected.

Inflammation-related gene expression

The expression levels of inflammation-related genes (Arg-1 and iNOS) were determined using real-time PCR. After incubating the cells with the AMRs for 24 h in DMEM medium, total RNA was extracted from cells using a modified Trizol protocol. RNA was quantified using a NanoDrop spectrophotometer (Thermo, USA). Complementary DNA (cDNA) was synthesized from RNA using a Prime Script RT Reagent Kit. Gene expression analysis was performed on a CFX96TM Real-Time PCR Detection System (Bio-Rad, USA) using SYBR Premix Ex Taq TM. PCR conditions were set as follows: initial denaturation at 95°C for 30 s, followed by 40 cycles at 95°C for 5 s; and 60°C for 30 s; melt curve from 65°C to 95°C with an increment of 0.5°C/5s. Levers of genes were normalized to GAPDH as a housekeeping gene. Cells cultured without samples were used as the control. Data were analyzed using the comparative 2-ΔΔct method. The experiment was performed in triplicate.

DOX loading and release from AMRs

DOX was loaded onto the AMRs via electrostatic interaction. Before drug loading, AMRs were modified by citrate. The reaction was performed by immersing the microrobot in 10 mM saline sodium citrate for 1 h, followed by removal of the free salt solution by washing with water. Then different concentrations of DOX were incubated with the citrate-modified AMRs at 37°C for 4 h. Then, supernatants containing non-loaded DOX were collected. The DOX-loaded AMRs in the pellet were washed twice with water and centrifuged at 5,000 rpm, and then resuspended in 1 mL of PBS for further use. The DOX concentration

in the supernatant solution was measured by UV–Vis spectra at λ = 480 nm. Drug loading efficiency (DLE) was determined as follows: DLE (wt %) = weight of loaded drug/weight of total AMRs.

Magnetic actuation and motion control

The locomotion performance of the AMRs was tested in a uniform rotating magnetic field generated by three orthogonal pairs of Helmholtz coils. Samples were placed in a 2 cm diameter polydimethylsiloxane (PDMS) chamber sealed with a glass coverslip to prevent evaporation. The magnetic field strength (mT) and rotational frequency (Hz) of the magnetic field were controlled by a LABVIEW program. Data analysis for the motion control experiments was performed by tracking the position of the microrobots over time in the recorded videos. A tracking algorithm written in MATLAB was used to process the captured videos and calculate the forward velocity of the AMRs.

Targeted treatment of 3D cancer cells spheroids by AMRs

Targeted anti-cancer cell therapy using dual targeting AMRs was assessed using 3D cancer cell spheroid models in a microfluidic channel. 3D cancer cell spheroids were generated using the matrigel and agarose, which are commonly used and commercially available ECM materials. First, agarose solution (1.5%, w/v) was prepared by heating at 121°C for 20 min; then, 60 μL of the agarose solution was coated on the bottom of the wells on a 96-well plate at 37°C for 30 min. Next, the 100 μL 4T1 cell suspension (500 cells) in 2.5% matrigel was added to the agarose-coated wells. The culture medium was half-changed every 3 days with the fresh medium. The formation of aggregates was monitored under the microscope and transferred to a microfluidic chip after the spheroids were formed. For experiments, the AMRs were placed inside the microfluidic chip with cell spheroids. The chip was then placed inside the Helmholtz coil system where the AMRs loaded with macrophage and DOX were magnetically guided to target the spheroids. When the AMRs got close to the spheroids, the magnetic field was stopped to allow the macrophage to specifically target the spheroids; simultaneously, the relatively acidic environment around the spheroids triggered DOX release. The effectiveness of the targeted cancer cell therapy was evaluated by observing the viability of the cancer cells in the spheroids through live/dead staining. Cell viability was evaluated using CCK-8 kit.

QUANTIFICATION AND STATISTICAL ANALYSIS

Data are represented as the mean ± SEM. P-values were calculated by one-way ANOVA test unless otherwise indicated. p values < 0.05 were considered significant. N = 3, where n denotes the number of times the data was replicated.